Combined Lattice–Boltzmann and rigid-body method for simulations of shear-thickening dense suspensions of hard particles

Lorenz, E.; Sivadasan, V.; Bonn, D.; Hoekstra, A.G.

DOI
10.1016/j.compfluid.2018.03.056

Publication date
2018

Document Version
Final published version

Published in
Computers and Fluids

Computers and Fluids 172 (2018) 474–482

Contents lists available at ScienceDirect

Computers and Fluids

journal homepage: www.elsevier.com/locate/compfluid

Combined Lattice–Boltzmann and rigid-body method for simulations of shear-thickening dense suspensions of hard particles

Eric Lorenz [a,b,*], Vishnu Sivadasan [a], Daniel Bonn [c], Alfons G. Hoekstra [a,d]

[a] Computational Science Lab, Institute for Informatics, Faculty of Science, University of Amsterdam, Netherlands
[b] Electric Ant Lab B.V., Amsterdam, The Netherlands
[c] Institute of Physics, Faculty of Science, University of Amsterdam, Netherlands
[d] ITMO University, Saint Petersburg, Russian Federation, Russia

ARTICLE INFO

Article history:
Received 31 October 2017
Revised 13 March 2018
Accepted 16 March 2018
Available online 17 March 2018

Keywords:
Lattice–Boltzmann
Rigid-body simulations
Suspensions
Adaptive timestep
Lees–Edwards boundary conditions
Shear thickening

ABSTRACT

We present a high-fidelity simulation model for dense suspensions of spherical and non-spherical particles suspended in a Lattice–Boltzmann Method (LBM) based fluid. The non-spherical particles are composed of an arbitrary number of overlapping spheres of different sizes and arbitrary relative positions in the particle reference frame which stay fixed during the simulation. This approach allows to approximate a wide range of rigid particle shapes. Fluid Structure Interactions (FSI) are realized using a hybrid of immersed-boundary methods and bounce-back schemes, that employs coupling coefficients dependent upon particle overlap with the fluid lattice, resulting in smooth hydrodynamic interactions when particles move over the lattice. Numerical lubrication breakdown is overcome by applying appropriate corrections for small inter-particle gaps and hydrodynamic interactions are resolved down to scales much smaller than the LBM lattice spacing. For improved numerical stability in the limit of stiff particle-particle interactions, a generalized-α method together with a dynamically refined time-step is used for rigid body dynamics. An unbounded shear flow with large shear rates is realized by splitting the computational domain into multiple co-moving reference frames coupled through Galilean transformations of both fluid and particle phase. For fast simulations of hundreds of particles over physical times-spans of seconds, the LBM sub-model and FSI computations are accelerated on GPUs and MPI/OpenMP are used to parallelize the computation over networked/shared-memory resources. All these innovations together lead to a very powerful simulation environment for sheared dense suspensions, facilitating study of rheology close to the jamming limit. In this paper we present benchmark results and simulations of continuous and discontinuous shear-thickening of dense polydisperse frictional suspensions, demonstrating the accuracy and predictive power of the model over a large range of volume fractions of suspended particles and a large range of shear rates.

1. Introduction

Shear thickening is the phenomenon in which the viscosity of a suspension increases as a function of the shear rate or shear stress imposed on the system. This is a commonly observed phenomenon in dense suspensions [1–4]. Two realms of shear thickening exist, continuous shear thickening(CST) and discontinuous shear thickening(DST). CST involves a gradual increase in the viscosity of the suspensions with shear rate while DST entails an orders of magnitude increase in viscosity with small increments in shear rate.

From recent experimental [5–8], and computational [9–11] results, the emerging agreement is that the stress induced transition of particle contacts from being lubricated and frictionless to being frictional is the underlying mechanism behind shear thickening, as originally suggested by Huang et al. [12].

The first viable model that could successfully reproduce both continuous and discontinuous shear thickening in the Stokes regime was published by Mari et al. [10], owing to the friction model introduced in their system that allows a transition between lubricated and frictional rheologies depending on a critical load. This model was recently validated experimentally [8]. Johnson et al. [13] presented a method to simulate shear thickening of frictional particles in an LBM based fluid by varying the boundary stiffness.

* Corresponding author.
E-mail addresses: e.lorenz@electricant.com (E. Lorenz), v.sivadasan@uva.nl (V. Sivadasan).

https://doi.org/10.1016/j.compfluid.2018.03.056
0045-7930/

In the model of Mari et al. [10] the fluid forces were approximated as a combination of drag force and pairwise lubrication interactions. The fluid phase was not modeled explicitly in their work. Recently, Johnson et al. [13] used LBM to explicitly model the fluid field and combined it with the Discrete Element Method to simulate shear thickening as a consequence of system dilation. This model was limited to low Reynold's number flows, and lubrication interactions were not resolved explicitly. Their simulations included the action of gravity, which according to Johnson et al. leaves the possibility of a flow segregation dependent on the shear rate or shear stress.

The model proposed in this paper uses accurate hydrodynamics from the particle scale down to scales much smaller than the LBM lattice spacing, owing to the advanced LBM fluid structure interactions (proposed by Noble and Torczynski [14]) and accurate corrections to the lubrication forces when the inter-particle gaps are smaller than the lattice spacing. We further improved numerical stability through an adaptive refinement of particle timesteps when the inter-particle gaps are small and the lubrication and other inter-particle forces diverge. The model is able to simulate polydisperse particle systems by sampling individual particle diameters from superpositions of normal distributions of particle sizes. The particles in the model can be spherical or any combination of overlapping spheres. This allows to generate and simulate a wide range of particle shapes approximating typical particle shapes found in real suspensions. The particles interact with each other using hydrodynamics and contact forces. The particle contacts involve normal and frictional (static and kinetic) forces. Lees–Edwards boundary conditions [15], and their extension to multiple layered reference frames are used to simulate bulk behavior in unbounded shear flow. The model is not limited to low Reynold's number flows which allows to simulate and study inertial flow regimes. Gravity is not considered in this model, so that its effects can be excluded from the discussion of the mechanisms behind shear thickening.

2. Models and methods

2.1. Fluid

2.1.1. Lattice Boltzmann Method (LBM)

LBM [16–18] is a numerical method in which the Boltzmann dynamics of fluid particles is discretized in space and velocity space. In the macroscopic limit it approximates the Navier–Stokes equations for viscous incompressible flow. Being rooted in kinetic theory however, various interactions other than those found in ideal gases can be incorporated in a natural way, making it possible to simulate non-ideal gases, emulsions and a variety of other fluids. Velocity distributions can be modified and quantities can be evaluated locally which is highly beneficial in the realization of boundary conditions at the surface of moving particles.

LBM makes use of a regular grid of lattice nodes with a lattice constant Δx and a finite number of velocity vectors pointing from one node to its nearest or next-nearest neighbors . We use a D3Q19 lattice [18] in this work. At each time-step, the particle density $f_i = f_i(\mathbf{x}, t)$ at each node $\mathbf{x}$ is evolved according to:

$$f_i(\mathbf{x} + \mathbf{e}_i \Delta t, t + \Delta t) = f_i(\mathbf{x}, t) + \Omega(\mathbf{f}) + F_i \tag{1}$$

where Ω is the collision operator used to reshuffle the velocities at a node, and F_i signifies the external forces (expressed in lattice units). In this work we use the LBGK collision operator that, using only one time-scale τ, relaxes the distributions $\mathbf{f}$ towards their equilibrium values according to the theory by Bhatnagar et al. [19]:

$$\Omega(\mathbf{f}) = \frac{1}{\tau}(\mathbf{f}^{\mathrm{eq}}(\mathbf{u}, \rho) - \mathbf{f}(\mathbf{x}, t)) \tag{2}$$

where $\mathbf{f}^{\mathrm{eq}}(\mathbf{u}, \rho)$ corresponds to the equilibrium distribution and the relaxation time τ can be related to the kinematic viscosity of the fluid ν. We refer the reader to [18] for the details. As explained in Section 2.8, the fluid phase simulations are executed on GPUs. Using single precision in GPUs however, has a few limitations associated with the reduced accuracy such as mass not being conserved and fluctuations in fluid-particle interaction forces due to local instabilities at large density gradients. This is due to the poor resolution in the representation of f_i when single precision is used. Skordos [20] proposed a technique to improve the numerical accuracy in this situation by rescaling the f_i values as the difference from the zero velocity equilibrium case (w_i) *i.e* $h_i = f_i - w_i$. From this, it follows that the LBGK equation (Eq. (1)) is translated to:

$$h_i(\mathbf{x} + \mathbf{e}_i \Delta t, t + \Delta t) = h_i(\mathbf{x}, t) + \Omega(h_i^{\mathrm{eq}} - h_i) + F_i \tag{3}$$

2.2. Particles

Particles are described as spheres or any combination of overlapping spheres (see Fig. 1) to approximate other particle shapes that are found in experimental systems. The interactions between particles (close to contact lubrication, particle contact, friction) are also modeled on this basis.

2.2.1. Particle-particle interactions

Apart from far and mid-range hydrodynamic interactions mediated through the LBM fluid field, the interactions between the particles include contact, frictional and explicit lubrication interactions.

Contact repulsion. If particle surfaces were perfectly smooth, lubrication interactions diverging in the limit of small gaps between two particles would prevent contact. However, real surfaces have a finite roughness and particles can make contact already at finite effective distances. It was recently found experimentally [8] that particle contacts become frictional if the inter-particle forces, either a result of potential or dissipative interactions, exceed a critical force, confirming this hypothesis. Before this critical load is reached, particles stay stabilized and well lubricated.

Two particles in our model are considered in contact if their inter-particle gap is smaller than a small contact layer thickness of $h_{\mathrm{cutoff}} = 0.1$ µm mimicking surface roughness (see Fig. 2). We have run simulations with various cutoff values and found that the chosen cutoffs are small enough to not impact the results through an increase of the effective volume of the particles. On the other hand, the cutoffs are also sufficiently large to render the interaction potentials soft enough for a stable numerical integration. The normal force $\mathbf{F}_{\mathrm{rep}}$ between the particles due to contact repulsion is modelled as:

$$\mathbf{F}_{\mathrm{rep}} = \begin{cases} -c\frac{(h-h_{\mathrm{cutoff}})^2}{h h_{\mathrm{cutoff}}^2}\mathbf{e}_h, & h \le h_{\mathrm{cutoff}} \\ 0 & \text{otherwise} \end{cases} \tag{4}$$

where c is the repulsion coefficient, h is the gap between the particles, and $\mathbf{e}_h$ is the connecting unit vector between the spheres. In the limit $h \to 0$ it diverges as $\sim h^{-1}$ preventing actual overlap of the particles. At $h = h_{\mathrm{cutoff}}$, $F_{\mathrm{rep}}(h_{\mathrm{cutoff}})$ and its first derivative $\partial_h F_{\mathrm{rep}}(h_{\mathrm{cutoff}})$ is zero. The latter is enforced in order to realize a smooth onset of the repulsion, further improving the numerical stability of the particle dynamics. Certainly in simulating very dense suspensions, such regularization to have a continuous and smooth onset of the repulsive force is required to obtain numerically stable dynamics. In the case of more complex particles built from multiple spheres, the repulsion is applied to each pair of spheres of both particles.

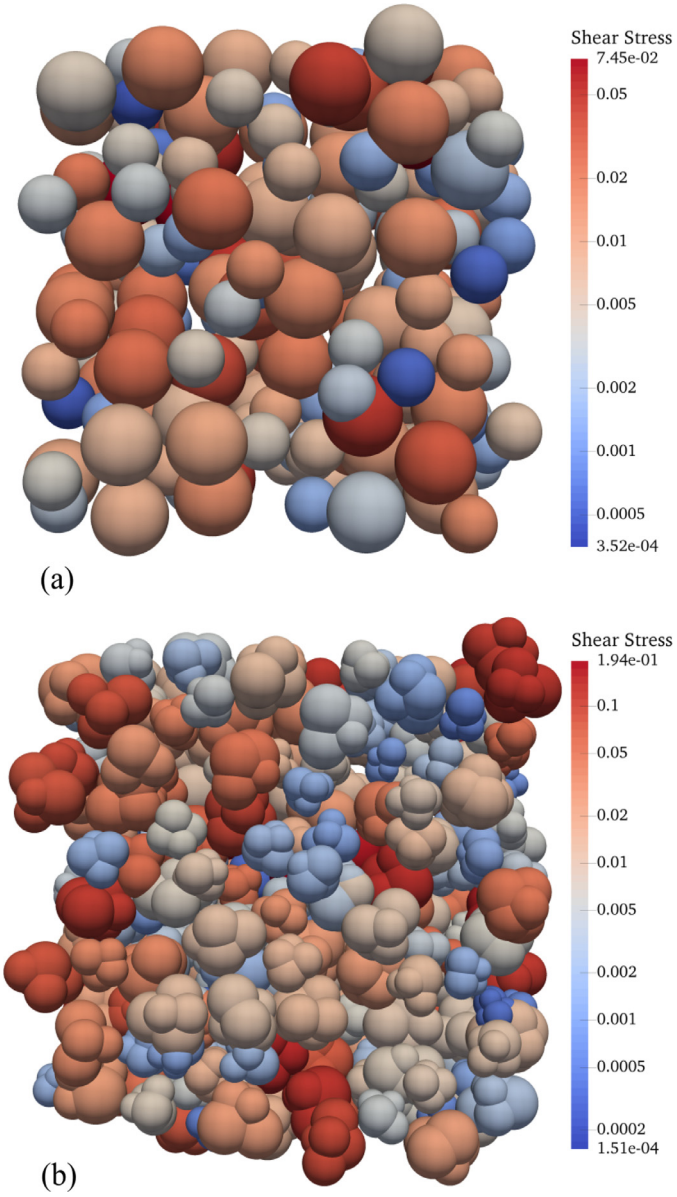

Fig. 1. Snapshots of a system with **(a)** spherical particles **(b)** non-spherical particles for $\phi = 0.5$, $\dot{\gamma} = 30.0$ /s. The colors represent the absolute shear stress on the particles in lattice units. (For interpretation of the references to color in this figure legend, the reader is referred to the web version of this article.)

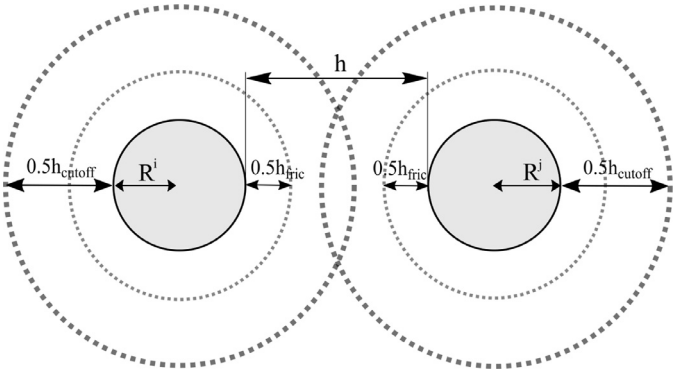

Fig. 2. Illustration of a typical spherical particle in the model (not to scale), of radius R^i and contact interaction cutoff h_{cutoff} and frictional interaction cutoff at h_{fric}.

Friction force. Both static and sliding friction, are modeled in a similar fashion to Luding [21]. The idea is that once two particle's friction interaction layers overlap, a linear spring of length ξ mimicking static friction will be initialized between the closest surface points and updated using the relative tangential velocity of the two surface points. Applying Coulomb's law, we say that the maximum static friction is $F_s \leq \mu_s |\mathbf{F}_{\text{norm, fric}}|$. If the amplitude of the spring force $\mathbf{F}_{\text{spr}} = -k\xi$ is smaller than the maximum possible static friction F_s then the spring force is applied. If it exceeds F_s, kinetic friction $F_k = \mu_k |\mathbf{F}_{\text{norm,fric}}|$ is applied as a tangential force at the surface points. In case of kinetic friction, the static friction spring is not broken, but its length is rescaled so that $F_{\text{spr}} = F_k$. This ensures a smooth transition back to static friction.

Critical load model. For particles in a suspension to interact frictionally, it is necessary to overcome stabilizing forces between the particles. It was found experimentally [8] that particles interact frictionally only if the inter-particle forces exceed a critical force. Before this critical load is reached, particles contacts remain lubricated and do not interact through friction.

In this work a minimal model of this mechanism is realized, called the Critical Load Model (CLM) [10]. If the normal force between two particle surfaces exceeds a critical load F_{CL}, a frictional contact can be established.

$$F_{\text{norm,fric}} = \begin{cases} |\mathbf{F}_{\text{rep}}| - F_{\text{CL}} & \text{if } |\mathbf{F}_{\text{rep}}| \geq F_{CL}, \\ 0 & \text{otherwise.} \end{cases} \tag{5}$$

The resulting $F_{\text{norm, fric}}$ from this model is then used as the normal force for the calculation of the friction. Since the contact repulsion is a potential interaction, a constant critical gap h_{fric} can be derived that defines a friction layer around the particles (see Fig. 2).

2.3. Fluid-structure interaction

Particles and fluid exchange forces at the surface of the particles, using the Noble–Torczynski method [14] for fluid structure interaction. It can be seen as a hybrid of standard LBM bounce-back methods and immersed-boundary approaches. In the Noble–Torczynski method (NT) the fractional overlap ϵ of a particle with a lattice node at $\mathbf{x}$ is used to calculate the particle-fluid interaction as an interpolation between free collision and bounce-back at the fluid nodes. The collision operator in the Lattice–Boltzmann equation then reads

$$\Omega_i = \left[1 - \sum_s B(\epsilon_s, \tau)\right] \Omega_i^{BGK} + \sum_s B(\epsilon_s, \tau) \Omega_i^s \tag{6}$$

where B is a function of the overlap ϵ_s with particle s. In this work, we have used

$$B(\epsilon_s, \tau) = \frac{\epsilon_s}{1 + \frac{1-\epsilon_s}{\tau - 0.5}}. \tag{7}$$

The collision operator in case of full overlap with the particle reads

$$\Omega_i^s = f^{\text{eq}}(\rho, \mathbf{U}_s) - f_i(\mathbf{x}, t) - (f_{-i}^{\text{eq}}(\rho, \mathbf{u}) - f_{-i}(\mathbf{x}, t)) \tag{8}$$

From this equation the exchanged momentum can be derived and the force on the particle 's' at $\mathbf{x}$ then reads

$$\mathbf{F}_s = \frac{\Delta x^3}{\Delta t} B(\epsilon_s) \sum_i \Omega_i^s \mathbf{e}_i \tag{9}$$

From this, the total hydrodynamic force and torque on the particle can be computed as a sum over all nodes $\mathbf{x}$ for which $\epsilon_s > 0$.

The fractional overlap ϵ_s is estimated using the assumption that the radius of a sphere within a particle is larger than Δx. This allows to estimate the partial overlap of a sphere with the cubic lattice node as an intersection of a plane (the particle surface) with

a cube (the lattice node). This is still a non-trivial calculation because of the many cases that need to be distinguished here and that make further assumptions necessary. A discussion of a validity of these assumptions however would overlap with a discussion of the shape and inner structure of a Lattice–Boltzmann node which is undefined. The calculations of ϵ_s is done at every time step for all lattice nodes $\mathbf{x}$ and particles s and takes about 25% of the total computing time. Since multiple particles can overlap with a single LBM node, a list of particles overlapping with that node stored together with their $\epsilon_s(\mathbf{x})$ and additional information such as local particle velocity $v_s(\mathbf{x})$ and distance to particle center $\mathbf{x} - \mathbf{r}_s$ that are necessary when total forces, torques and stresses are computed.

The NT method has a number of advantages for simulations of dense suspensions with stiff interactions, the need for consistent lubrication corrections, and using a multiple Lees–Edwards approach explained in Section 2.6. In the majority of works combining LBM and rigid particles the momentum exchange method by Ladd [22,23] and the methods proposed by Aidun et al. [24] are applied which are based on bouncing back probability density f's at links that intersect the fluid-particle interface. In this case, the underlying binary stair-case representation of particles on the fluid lattice, i.e. ϵ being either 1 or 0, leads to peaks in the exchanged momentum when a fluid node turns solid and vice versa [25]. In this situation also the momentum from the removed or created fluid needs to be exchanged with the particle. In the stiff interaction limit of dense suspensions in dynamical jamming situations such discontinuities would quickly lead to numerical stability problems. We also find that the lubrication breakdown using the NT method is rather consistent, i.e. not dependent on the lattice positions of the two close particles and can therefore be corrected in a much more consistent way, see Section 2.3.1. The NT FSI is also more consistent than immersed-boundary methods which tend to overestimate lubrication interactions depending on the lattice position of the particles (or mesh points in that case), see [26].

2.3.1. Explicit lubrication corrections

Below a certain threshold gap, the lubrication force calculated from LBM is no longer accurate, and tends to stay constant [27] (see Fig. 3). Using the explicit calculation of lubrication forces [28], we can calculate corrections to the lubrication forces from LBM if the inter particle gap h is below a threshold gap h_c. Similar to but slightly improving over the lubrication corrections proposed in [27], we use the following form for normal lubrication force

$$\mathbf{F^n}_{\text{lub}} = 6\pi\eta \frac{R_1^2 + R_2^2}{(R_1 + R_2)^2} \frac{(h - h_c)^2}{h h_c^2} U_n \cdot \hat{\mathbf{n}}, \quad h \le h_c \tag{10}$$

Similarly, the corrections to the tangential lubrication force for the rotational motion of a sphere past another [28] is expressed as

$$\mathbf{F^t}_{\text{lub}} = 8\pi\eta R_1 \frac{\beta(4+\beta)}{10(1+\beta)^2} \left(\log\left(\frac{h}{h_c}\right) - \left(\frac{h}{h_c} - 1\right) \right) U_t \cdot \hat{\mathbf{t}}, \quad h \le h_c \tag{11}$$

where $\beta = R_2/R_1$, R_1, R_2 being particle radii. η is the fluid viscosity. U_n and U_t corresponds to the normal and tangential relative velocities of the particles at the closest surface points. $\hat{\mathbf{n}}$ and $\hat{\mathbf{t}}$ are unit vectors in the corresponding normal and tangential directions.

These forms of lubrication correction are modified so that both, their values as well as their first derivative, are continuous functions of the gap which contributes to the numerical stability of the time integration. In the range of small gaps, these corrections approximate analytical solutions well, as shown in Figs. 3 and 4.

In Fig. 3, we compare the hydrodynamic normal force between two approaching spherical particles of radius $R = 8$ µm at various interparticle gaps for a set of lattice spacings (Δx) to the analytical solutions to long and short range hydrodynamic interactions.

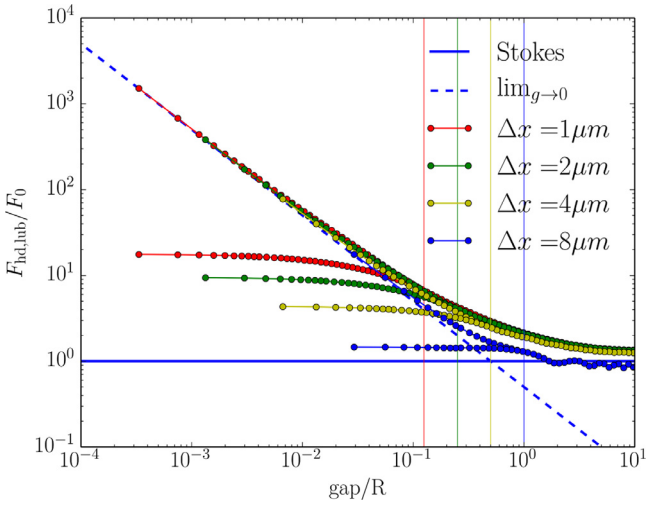

Fig. 3. Normal force between approaching spheres in a fluid medium with sphere radius $R = 8$µm and fluid viscosity $\eta = 1.002 \times 10^{-3}$ Pa s at various gaps for different lattice spacings (Δx). The forces are normalized by the drag on an isolated sphere, $F_0 = 6\pi\eta R U_n$. The vertical lines indicate the corresponding h_c. The result of the lack of application of the lubrication correction are shown, as the forces become constant at smaller gaps. With the application of the lubrication corrections, the simulation approximates the analytical solutions better. Analytical solutions to Stokes drag force at long gaps and lubrication interactions at short gaps (lim$_{g\to 0}$) are also shown.

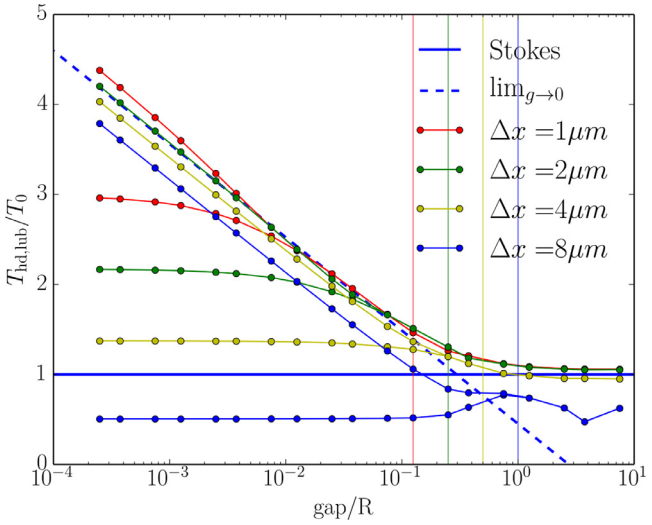

Fig. 4. Torque between two rotating spheres at various particles gaps in a fluid medium with sphere radius $R = 8$ µm and fluid viscosity $\eta = 1.002 \times 10^{-3}$ Pa s at various gaps for different lattice spacings (Δx). The torques are normalized by the torque on an isolates sphere, $T_0 = 8\pi\eta\omega R^3$. The vertical lines indicate the corresponding h_c. The effects of the lack of application of the corrections are shown, as the torques becomes constant at smaller gaps. With corrections applied, the model approximates the analytical solution well for sufficiently small lattice spacings Δx.

The vertical lines indicate the cutoff $h_c = 1\Delta x$. The hydrodynamic forces plateauing without lubrication corrections is also shown in the figure. With corrections applied, the interparticle forces approximate well the analytical solutions at smaller gaps. In the limit of large gaps, hydrodynamic forces on the particles converge to the Stokes situation of a single particle dragged through a viscous fluid. Deviations can be attributed to the finite size of the periodic simulation domain in which particles interact through many copies of the other particle and themselves.

In Fig. 4, we compare the hydrodynamic torque between two rotating spheres ($\omega = 100$ rad/s) at different interparticle gaps for different lattice spacings (Δt). In the long ranges, the torque on

a rotating sphere is given by $T_{\text{Stokes}} = 8\pi\mu R^3\omega$, and in the short ranges, the torque on particle 1 due to the lubrication interaction between particle 1 and particle 2 is given by,

$$\mathbf{T}_{\text{lub}} = 8\pi\eta\omega R_1^3 \frac{2\beta}{5(1+\beta)} \log\left(\frac{R_1}{h}\right) \tag{12}$$

It is seen that the model approximates the analytical solutions for large gaps, and in the short gaps the model is consistent with analytical solution for small enough lattice spacings.

2.4. Particle stresses

The mean value of the stress $\boldsymbol{\sigma}$ over a body of volume V can be calculated directly from the forces over the surface without solving the equilibrium stress distribution inside the solid [29] In the simulations, the mean stresses inside a particle s due to hydrodynamic interactions on its surface is estimated by a sum of the local stress over all fluid nodes with a non-zero ϵ_s.

$$\langle\sigma_{ij,s}\rangle(t) = \frac{1}{2V_s}\sum_{\mathbf{x}} \epsilon_s(F_i(\mathbf{x},t)r_j + F_j(\mathbf{x},t)r_i) \tag{13}$$

Where $\mathbf{r} = \mathbf{x} - \mathbf{r}_s$ is the vector from the center of mass of the particle to the point of action of force. Because the virtual fluid inside the particle is pinned to the movement of the solid matrix, the stresses evaluated inside the particle are negligibly small.

Similarly, but using a single term, mean stresses due to interactions $\mathbf{F}^{(su)}$ between particles s and particle u, such as lubrication corrections, repulsion and friction, are evaluated as

$$\langle\sigma_{ij,s}^{(su)}\rangle(t) = \frac{1}{2V_s}\left(F_i^{(su)}(t)r_j^{(cs)} + F_j^{(su)}(t)r_i^{(cs)}\right)$$

with $\mathbf{r}^{(cs)}$ being the point of action on the surface of particle s relative to the particle's center of mass.

2.5. Rigid body dynamics

Since non-spherical particles are also modeled, we employ a full rigid-body description of the dynamics of the particles (see [30,31] for an introduction to rigid-body dynamics). The inertia tensor $\mathbf{I}_\text{b}$ of each particle in the reference frame of the particle's principle axes i, j, and k is computed as a pre-processing step by first numerically evaluating

$$I_{\text{b},i} = \int_V \rho(\mathbf{r})(r_{p,j}^2 + r_{p,k}^2)\,\mathrm{d}V \tag{14}$$

with $\mathbf{r}_{p,<ijk>}$ being a point in the particle reference frame and $\rho(\mathbf{r})$ being either ρ_{solid} or 0 depending on whether $\mathbf{r}$ is inside or outside the particle, respectively.

The rotational state of a particle is represented using quaternions. This choice makes it necessary to derive rotation matrices from quaternions in order to compute inertia tensors and rotational states in the world frame, however, no numerical instabilities or drift occurs that are associated with the singularities of the rotation group SO(3) when using three angles to represent the rotational state.

Updates of the particle's translational and rotational state are performed using the explicit generalized-α method using the parameters proposed in Hulbert et al. [32]. The update is second-order accurate and parameters are such that non-physical high-frequency modes on the time-scale of the particle update are efficiently damped.

The algorithm for the translational state is as follows. First, the acceleration at the new time step $t + \Delta t$ is computed as

$$\ddot{\mathbf{r}}(t+\Delta t) = \frac{\mathbf{F}/m - \alpha_m\ddot{\mathbf{r}}(t)}{1-\alpha_m} \tag{15}$$

Additionally, the acceleration is evaluated at two different times between t and $t + \Delta t$.

$$\ddot{\mathbf{r}}_\beta = \left(\frac{1}{2} - \beta\right)\ddot{\mathbf{r}}(t) + \beta\ddot{\mathbf{r}}(t+\Delta t) \tag{16}$$

$$\ddot{\mathbf{r}}_\gamma = (1-\gamma)\ddot{\mathbf{r}}(t) + \gamma\ddot{\mathbf{r}}(t+\Delta t) \tag{17}$$

Using these approximated accelerations, position and velocity of the particle are updated following

$$\mathbf{r}(t+\Delta t) = \mathbf{r}(t) + \Delta t\dot{\mathbf{r}}(t) + \Delta t^2\mathbf{a}_\beta \tag{18}$$

$$\dot{\mathbf{r}}(t+\Delta t) = \dot{\mathbf{r}}(t) + \Delta t\mathbf{a}_\gamma \tag{19}$$

The inter/extra-polation parameters are functions of a single damping parameter λ.

$$\alpha_m = \frac{2\lambda - 1}{1+\lambda} \tag{20}$$

$$\beta = \frac{5-3\lambda}{(1+\lambda)^2(2-\lambda)} \tag{21}$$

$$\gamma = \frac{3}{2} - \alpha_m \tag{22}$$

The update of the rotational state has the same structure. In it, the inertia tensor plays the role of mass and its inverse in global reference frame can be computed as

$$\mathbf{I}^{-1}(t) = \mathbf{R}(\mathbf{q}(t)) \cdot (\mathbf{I_b}^{-1} \cdot \mathbf{R}^T(\mathbf{q}(t))) \tag{23}$$

where $\mathbf{q}(t)$ is the quaternion describing the rotational state at time t an $\mathbf{R}$ is the corresponding rotation matrix.

The angular velocity ω and acceleration α can be calculated as $\omega = \mathbf{I}^{-1} \cdot \mathbf{L}$ and $\alpha = \mathbf{I}^{-1} \cdot \mathbf{T}$, respectively, with $\mathbf{L}$ and $\mathbf{T}$ being the angular momentum and torque. The rotation matrix $\mathbf{R}$ can be computed from the quaternion representing the rotational state of the particle.

2.6. Multiple Lees Edwards reference frames

Lees–Edwards boundary conditions are a common approach to simulate sheared flow in quasi infinite systems and are therefore the appropriate choice for studies of bulk rheological properties in the absence of walls. Implementation of Lees–Edwards boundary conditions in an LBM framework, however, introduces a limit on the shear rates as the fluid velocity, in lattice units, is bound to low Mach numbers. As a result, either the system size in velocity gradient direction or the Reynolds numbers are limited.

This limit can be shifted to N_L times larger shear rates by decomposing the domain into N_L Lees–Edwards layers in shear-gradient direction, each with their own reference frames where the above mentioned constraints apply (see Fig. 5). These reference frames are co-moving with the shear flow, with small velocities in lattice units. At the interface of these domains, Galilei transformations are applied as proposed in Wagner et al. [33] for the LBM subsystem, and in Lorenz et al. [15] where it also has been applied to suspended particles. Because fluid–solid boundary conditions were applied to LBM probability densities (f) in [15] during the streaming step, interpolation and transformations had to be applied selectively to streamed f's depending on whether they would bounce back into their original reference frame or not. In the current work, a node-local boundary condition is used and f's can be streamed and transformed independently from fluid–solid boundary conditions which simplifies the situation significantly. In order to complete a fully periodic boundary setup with multiple Lees–Edwards reference frames, the top interface of uppermost layer is linked to the bottom of the lowermost layer.

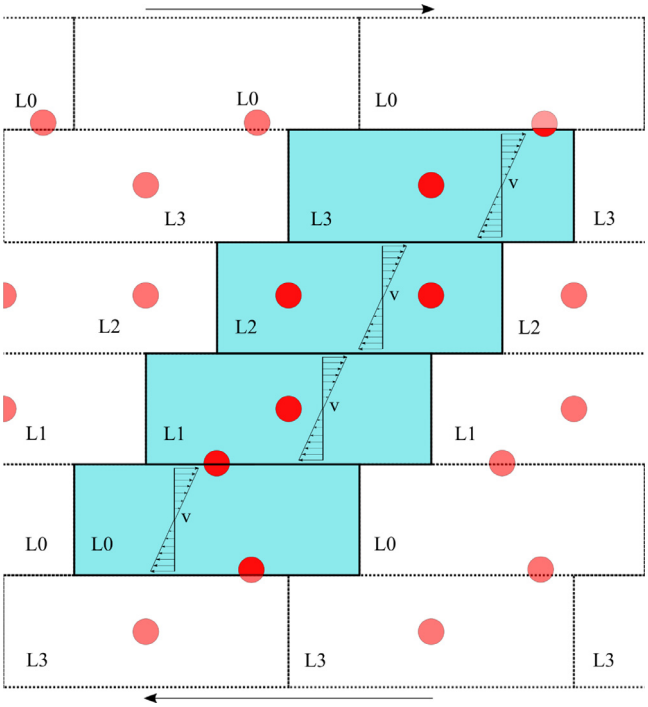

Fig. 5. Lees Edwards Boundary conditions, with periodic copies moving past each other with their own reference frames. The individual layers are marked as L0, L1, L2 and L3. The local fluid velocities in the individual reference frames are shown.

2.7. Adaptive time-step refinement

At small gaps, the lubrication force and the contact forces between the particles diverge. In situations where shear stresses are large enough that particles overcome stabilizing interactions and therefore inter-particle gaps become very small, this potentially leads to numerical instabilities of the particle time integration. The obvious solution is to decrease the time step. Feng et al. [34] proposed to precompute a constant sub-cycling factor between fluid and particle timesteps, Δt_{LBM} and Δt_{solid} based on the critical damping of a spring-damper system using the contact forces $|\mathbf{F}_{\text{rep}}|$. Lubrication and contact forces diverge as $\sim \dot{r}/r$ and $\sim 1/r$ leading to a non-trivial non-linear mixed-order ODE stability problem when combined with an explicit integration. Also, for dynamically jamming particle systems the interaction strength cannot be easily predicted from the typical stresses. We therefore chose to dynamically adapt the particle time-step Δt_{solid} based on an estimate of the numerical stability of the integration. Doing so, time-steps are large when the stresses in the system are low and only become small when particles interact heavily as during jamming. There is no limitation of the subcycling factor. This allows to simulate close to jammed systems. Of course, computational costs increase in these situations.

The dynamical subcycling is applied to particle dynamics and the evaluation of all inter-particle forces including the lubrication corrections. Forces and torques from hydrodynamic interactions through the fluid field, which have no divergence and change rather smoothly on the fluid timescale Δt_{LBM} (see Section 2.3), are estimated as a linear extrapolation using $\mathbf{F}_{\text{hd}}$ and $\mathbf{T}_{\text{hd}}$ evaluated at the last two full fluid timesteps. Other simple predictor schemes have been tested without observing significant deviations and we found that the method used here results in smooth hydrodynamic forces and torques.

The subcycling factor is evaluated and applied globally (i.e. for all particles). Extensions of this scheme where an optimal timestep is determined dynamically for each particle or particle pair are possible but would make synchronization of the particles necessary which would result in increased overhead for handling and communication in parallel simulations.

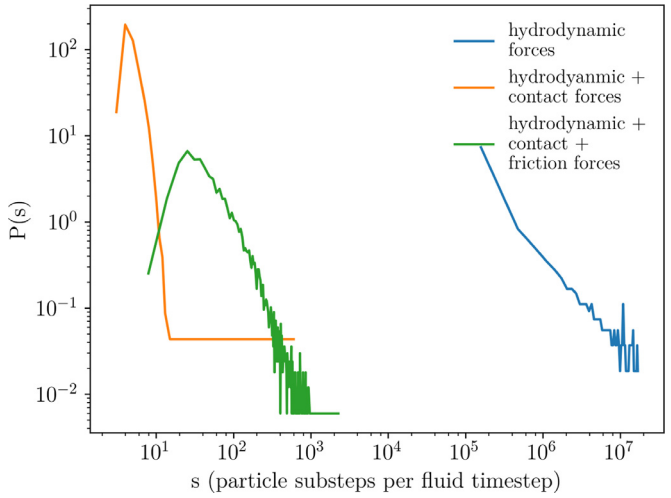

Fig. 6. Normalized histograms of the particle substeps per fluid timestep in simulations for three cases (a) only hydrodynamic forces, (b) hydrodynamic forces and contact forces, (c) hydrodynamic, contact and frictional forces, where $\phi = 0.5$, $\dot{\gamma} = 10^3 s^{-1}$. The Y axis has been normalized by the sample sizes of the respective cases.

In this work, adaptive refinement of particle timesteps is based on Fourier "sensors" on the particles linear and rotational accelerations. Fourier modes of acceleration of particles are tracked, and if onsets of oscillations in the time signals of acceleration are found, the particle timesteps are reduced or increased accordingly. Adaptation of the particle timesteps is done by observing simple estimates of the first four high-frequency coefficients $c(k)$ of a simple discrete Fourier series using the last $h_{\max} = 4$ values of translational and rotational particle acceleration, $a(t)$ and $\alpha(t)$, which need to be stored and updated for each particle at each particle time step. The coefficients for translational accelerations are determined as

$$c_p^a(k) = \sum_{h=0}^{h_{\max}-1} a_p(t-h) \cos\left(\frac{2\pi kh}{h_{\max}}\right) \tag{24}$$

and in a similar way for the rotational accelerations α_p.

The maximum coefficient $c_{\max}(t)$, which is determined over all particles, wave numbers $k = 1..h_{\max}$, and acceleration types a and α, is then used to set the new timestep according to

$$\Delta t_{\text{solid}} = \left(\frac{c_{\text{ceiling}}}{c_{\max}(t)}\right)^e \Delta t. \tag{25}$$

In it, c_{ceiling} defines the maximum tolerated Fourier coefficient. For the simulations in this work, we find that $c_{\text{ceiling}} = 10^{-8}$ (in simulation units) results in a good compromise between fast integration (with large timesteps) and stability (small timesteps). The exponent e in Eq. (25) defines how fast the timestep is changed. We found that $e = 0.05$ is an appropriate choice to adapt the timestep quick enough to suppress numerical oscillations that build up in situations with stiff particle interactions on one hand, and slow enough to prevent overshooting in this adaptive scheme on the other.

In Fig. 6, histograms of the subcycling factor (s) are shown for three different cases of particle-particle interactions. In the first case, we have only hydrodynamic and lubrication interactions between particles and no contact or friction. In this case, heavy particle subcycling is observed, as the particles get closer because of the lack of stabilizing forces. This large subcycling behavior resonates with the observations of Melrose et al. [35], who proposed

that there is no steady state numerical solution for a purely viscous flow. This is because there is no other way for a gap between particles to bear compressive load than to shrink, which leads to increasingly smaller gaps, diverging lubrication interactions, and an increase of the particle timestep subcycling. Because in flowing systems the interactions between particle pairs (compressive, tensile) will change during the evolution of the microstructure on finite time-scales, typical particle gaps have a finite lower limit and the subcycling stays finite. We also observed situations in which the subcycling became so heavy that within finite computing time we could not judge whether the system was still flowing or (physically) jammed. In the next case, where contact forces are added, we observe that particle subcycling is significantly reduced as expected. Finally, when friction is also introduced into this system, it is observed that the subcycling increases again as a consequence of frictionally arrested particles, its associated dissipation, and consequently smaller inter-particle gaps.

2.8. Parallelization

The simulation code is written in modern Fortran (F2008) and parallelized using three different approaches. In shear-gradient direction the computational domain is decomposed into subdomains with their own reference frame as described in Section 2.6 that are handled by one MPI process each. These MPI processes can be distributed over a number of compute nodes. Galileian transformations of the LBM and particle subsystems are applied during the communication step. Communication envelope of the D3Q19 LBM subsystem is $1\Delta x$ wide while for the particle system it is chosen such that all information is available for interaction of particle pairs that lie across an interface. Within each subdomain (i.e. MPI process) computation of the LBM subsystem including mapping of the particles onto the lattice and FSI is carried out on GPGPU's using OpenCL (through the FortranCL wrapper [36]). Running multiple MPI processes per compute node allows to use multiple GPU cards on each node. The locality of LBM on a structured grid of thousands to millions of nodes and the node-local FSI method (see Section 2.3) is well suited for GPU computing, see e.g. [37]. For pure single-phase fluid problems a speed-up of about 20 can be achieved through OpenCL parallelization on a Nvidia GTX1080, including all overhead such as host-GPU communication which takes approximately 20% of the total execution time, compared to a similar implementation on one core of an Intel i7-4770K CPU. The computations of particle-particle interactions and dynamics are distributed over multiple OpenMP threads on the host CPU using the standard approach of spatially binning particles into grid nodes of the size of at least the maximum interaction range (reducing the N_p^2 scaling of the many-body problem to $N_n N_{pn}^2$ with the total number of particles N_p, the number of grid nodes N_n, and the average number of particles per grid node N_{pn}). The number of particles per subdomain is too low (max a few hundred) and the interaction neighborhood of moving particles is too unstructured to gain any speedup from using GPUs for the particle subsystem. Also, most of the computations on GPU (LBM, FSI) and CPU (particle interactions, dynamics) can run in parallel this way. Naturally, the load on the CPU scales with the momentary particle timestep subcycling factor while the GPU load from the fluid subsystem with a constant timestep stays practically constant, so in case of jammed dense suspensions the load on CPU can increase far beyond the GPU load. Since the subdomains do not change their size during a simulation, inhomogeneous distributions of particles can potentially lead to load imbalances between subdomains [38,39]. This was not observed for the dense systems studied in this work. The complexity of the physical system, adaptive numerical solvers and the parallelization scheme results in various non-trivial dependencies influencing parallel performance which will be discussed in a future publication.

Table 1
System parameters used for simulation.

System dimensions	64 µm × 48 µm × 64 µm
Particle size	8 µm (50%), 11.2 µm (50%)
Particle standard deviation	0.1 µm
Static friction coefficient (μ_s)	1.0
Kinetic friction coefficient (μ_k)	1.0
Contact interaction distance (h_{cutoff})	0.1 µm
Contact repulsion coefficient (c)	10^{-16}Nm
Critical Load (F_{CL})	0.2 nN
Fluid Viscosity (η_f)	$1.002{\cdot}10^{-3}$ Pa s
Max. Strain	10
Δx_{LBM}	1 µm
Lubrication correction threshold gap (h_c)	1 µm

3. Results

3.1. Spherical particles

Simulations of shear thickening suspensions were performed on a system 64 µm × 48 µm × 64 µm. The diameter of the particles were distributed in a binormal distribution with peaks at 8 µm and 11.2 µm, with a standard deviation of 0.1 µm. This distribution of particles with a size ratio of 1.4 is commonly used in the literature to avoid ordering and crystallization effects found in monomodal distributions [10,40,41]. For simulating dense suspensions, the volume fraction (ϕ) is varied between 0.4 and 0.56, resulting in number of particles in the system ranging between 180 and 250 depending on the volume fraction. The shear rates are varied between 1 /s and 1000 /s. The particles have a contact interaction distance of $0.01a \approx 0.1$ µm. The critical load value for friction was set to 0.2 nN so as to have frictional contacts around a shear rate of 10 /s for $\phi = 0.56$. The relevant simulation parameters are given in Table 1.

We compared the viscosity at near zero shear rates against the Krieger Dougherty prediction for zero-shear viscosity [42] for spherical particles:

$$\eta_r = \left(1 - \frac{\phi}{\phi_{\max}}\right)^{-2.5\phi_{\max}} \tag{26}$$

where η_r is the relative viscosity and $\phi_{\max}$ is the maximum packing fraction. A maximum packing fraction of $\phi_{\max} = 0.646$ was calculated for the bimodal distribution as shown by Dames et al. [43], instead of the random close packing $\phi_{\max}^{\text{rcp}} = 0.64$ for monomodal distributions. The results of the simulations match the Krieger–Dougherty predictions quite well (see Fig. 7). In the limit of small ϕ, the Krieger–Dougherty relation as well as the numerical results converge to Einstein's viscosity [44,45] $\eta_r = 1 + 2.5\phi$ (data for $\phi < 0.2$ not shown).

At lower shear rates, the system stays in a Newtonian flow regime where the viscosity remains constant over the shear rates. The system shear thickens at higher shear rates, as evident from Fig. 8. For lower volume fractions, we observe a continuous increase in the relative viscosities, signifying CST, and at higher volume fractions, we observe orders of magnitude increase in relative viscosities over a small shear rate change, characteristic of DST. These results are in agreement with the results of Mari et al. [10].

3.2. Non spherical particles

Simulations of shear thickening were performed for non spherical particles created by overlapping 5 spherical particles (see Fig. 1). The longest diameter of the non spherical particles adhere

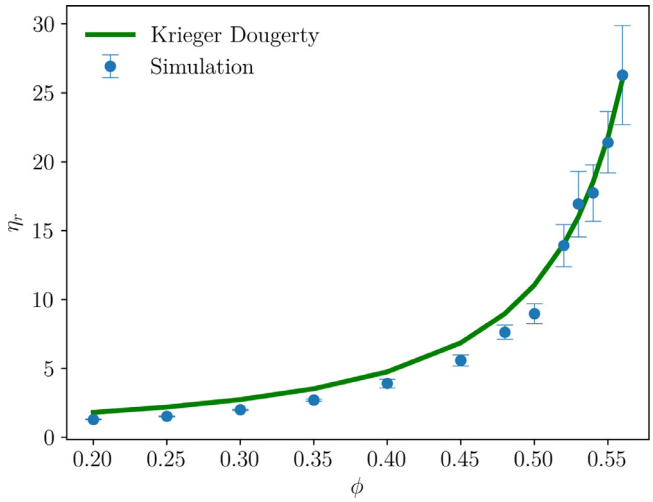

Fig. 7. Krieger Dougherty prediction vs. simulation results for $\phi_{max} = 0.646$. The error bars correspond to the oscillations in the viscosity timeseries of the individual simulations.

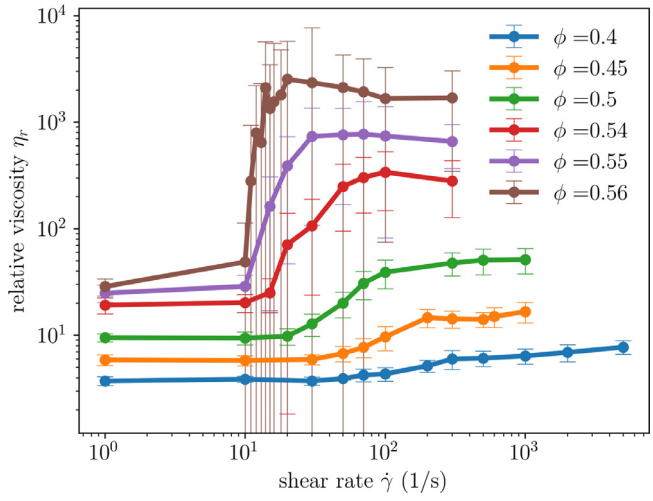

Fig. 8. Relative viscosity (η_r) (time averaged) vs. Shear rate ($\dot{\gamma}$) for different particle volume fractions (ϕ).

to the particle size distribution used for the spherical particles in Section 3.1. All the other properties of the particles and the fluid matches that of the spherical particle's case.

We observed that in the system of non spherical particles, shear thickening is stronger for a given volume fraction compared to that of the spherical particle system. In Fig. 9, we see that for $\phi = 0.45, 0.50$ cases, the non spherical particle system has higher relative viscosities compared to that of a spherical particle system with the same volume fraction. This increased shear thickening associated with non spherical particles has been reported before in experimental systems [46,47] as well. This could be attributed to the lower jamming particle volume fractions that were observed for non spherical particles in our system. A detailed analysis is the topic of future work.

4. Conclusion

We have successfully reproduced shear thickening by using Lagrangian particles in an LBM fluid. The particle phase uses accurate contact and frictional interactions to model particle-particle interaction dynamics. Multiple spherical particles can be overlapped to create a wide range of particle shapes to approximate real non-

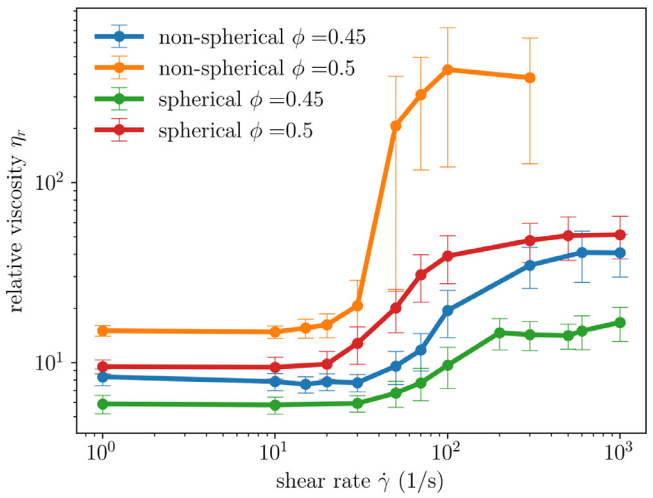

Fig. 9. comparison of the relative viscosity vs. shear rate curves for spherical and non spherical particles.

spherical particles in suspensions. A quaternion based description of the particle dynamics is used to simulate the motion of non spherical particles effectively. Explicit lubrication corrections are applied , and particle timestep sub-cycling is used to ensure numerical stability and accuracy. Noble–Torczynsky method, which overcomes the limitations of the Ladd's method is used for the fluid structure interaction. Lubrication benchmarks for Noble Torczynsky method is presented for the first time. Finally, shear simulations were performed on both spherical and non spherical particles and shear thickening was observed in both the cases. The model opens the possibility to explore shear thickening in different systems by virtue of its efficiency, accuracy and robustness. It is possible to add more interactions to the model (electrostatic, magnetic) between the particles to simulate different types of suspensions. These works are underway [48] and will be discussed in the following publications.

Author contributions

EL and VS contributed equally to this paper. EL designed and implemented the original model, VS added the Critical Load model for friction, and carried out all simulations and associated analyses. VS wrote the paper. EL, DB, and AgH conceived the research and guided the reported simulations, and reviewed and improved the manuscript. The authors declare no conflict of interest.

Acknowledgments

We would like to thank SURFsara for using their HPC infrastructure and for providing support (project number 00231267). Author VS acknowledges funding by NWO, Netherlands under the CSER program (project number 14CSER026).

References

[1] Fall A, Bertrand F, Ovarlez G, Bonn D. Shear thickening of cornstarch suspensions. J Rheol 2012;56:575–91.
[2] Fall A, Bertrand F, Hautemayou D, Mezière C, Moucheront P, Lemaître A, Ovarlez G. Macroscopic discontinuous shear thickening versus local shear jamming in cornstarch. Phys Rev Lett 2015;114:1–5.
[3] Brown E, Forman NA, Orellana CS, Zhang H, Maynor BW, Betts DE, DeSimone JM, Jaeger HM. Generality of shear thickening in dense suspensions. Nat Mater 2010;9:220.
[4] Brown E., Jaeger H.M. Shear thickening in concentrated suspensions: phenomenology, mechanisms, and relations to jamming. 2013.
[5] Lin NY, Guy BM, Hermes M, Ness C, Sun J, Poon WC, Cohen I. Hydrodynamic and contact contributions to continuous shear thickening in colloidal suspensions. Phys Rev Lett 2015;115:228304.

[6] Pan Z, de Cagny H, Weber B, Bonn D. S-shaped flow curves of shear thickening suspensions: direct observation of frictional rheology. Phys Rev E 2015;92:032202.
[7] Royer JR, Blair DL, Hudson SD. Rheological signature of frictional interactions in shear thickening suspensions. Phys Rev Lett 2016;116:188301.
[8] Comtet J, Chatté G, Niguès A, Bocquet L, Siria A, Colin A. Pairwise frictional profile between particles determines discontinuous shear thickening transition in non-colloidal suspensions. Nat Commun 2017;8:15633.
[9] Seto R, Mari R, Morris JF, Denn MM. Discontinuous shear thickening of frictional hard-sphere suspensions. Phys Rev Lett 2013;111:1–5.
[10] Mari R, Seto R, Morris JF, Denn MM. Shear thickening, frictionless and frictional rheologies in non-Brownian suspensions. J Rheol 2014;58:1693–724.
[11] Ness C, Sun J. Shear thickening regimes of dense non-Brownian suspensions. Soft Matter 2015;12:914–24.
[12] Huang N, Ovarlez G, Bertrand F, Rodts S, Coussot P, Bonn D. Flow of wet granular materials. Phys Rev Lett 2005;94:028301.
[13] Johnson DH, Vahedifard F, Jelinek B, Peters JF. Micromechanical modeling of discontinuous shear thickening in granular media-fluid suspension. J Rheol 2017;61:265–77.
[14] Noble D, Torczynski J. A Lattice–Boltzmann method for partially saturated computational cells. Int J Modern Phys C 1998;9:1189–201.
[15] Lorenz E, Hoekstra AG, Caiazzo A. Lees–Edwards boundary conditions for lattice Boltzmann suspension simulations. Phys Rev E 2009;79:036706.
[16] Succi S. The lattice Boltzmann equation: for fluid dynamics and beyond. Oxford University Press; 2001.
[17] Chen S, Doolen GD. Lattice Boltzmann method for fluid flows. Annu Rev Fluid Mech 1998;30:329–64.
[18] Krüger T, Kusumaatmaja H, Kuzmin A, Shardt O, Silva G, Viggen EM. The lattice Boltzmann method. Springer; 2017.
[19] Bhatnagar PL, Gross EP, Krook M. A model for collision processes in gases. I. Small amplitude processes in charged and neutral one-component systems. Phys Rev 1954;94:511.
[20] Skordos P. Initial and boundary conditions for the lattice Boltzmann method. Phys Rev E 1993;48:4823.
[21] Luding S. Cohesive, frictional powders: contact models for tension. Granular Matter 2008;10:235–46.
[22] Ladd AJ. Numerical simulations of particulate suspensions via a discretized Boltzmann equation. Part 1. Theoretical foundation. J Fluid Mech 1994;271:285–309.
[23] Ladd AJ. Numerical simulations of particulate suspensions via a discretized Boltzmann equation. Part 2. Numerical results. J Fluid Mech 1994;271:311–39.
[24] Aidun CK, Lu Y, Ding EJ. Direct analysis of particulate suspensions with inertia using the discrete Boltzmann equation. J Fluid Mech 1998;373:287–311.
[25] Lorenz E, Caiazzo A, Hoekstra AG. Corrected momentum exchange method for lattice Boltzmann simulations of suspension flow. Phys Rev E 2009;79:036705.
[26] Mountrakis L, Lorenz E, Hoekstra A. Revisiting the use of the immersed-boundary Lattice–Boltzmann method for simulations of suspended particles. Physical Review E 2017;96:013302.
[27] Nguyen NQ, Ladd A. Lubrication corrections for Lattice–Boltzmann simulations of particle suspensions. Phys Rev E 2002;66:046708.
[28] Kim S, Karrila SJ. Microhydrodynamics: principles and selected applications. Courier Corp; 2013.
[29] Landau LD, Lifshitz E. Theory of elasticity. Course of Theor Phys 1986;7(3):109.
[30] Baraff D. An introduction to physically based modeling: rigid body simulation I - unconstrained rigid body dynamics. SIGGRAPH Course Notes 1997.
[31] Baraff D. An introduction to physically based modeling: rigid body simulation II - nonpenetration constraints. SIGGRAPH Course Notes 1997:D31–68.
[32] Hulbert GM, Chung J. Explicit time integration algorithms for structural dynamics with optimal numerical dissipation. Comput Methods Appl Mech Eng 1996;137:175–88.
[33] Wagner AJ, Pagonabarraga I. Lees–edwards boundary conditions for lattice Boltzmann. J Stat Phys 2002;107:521–37.
[34] Feng Y, Han K, Owen D. Combined three-dimensional lattice Boltzmann method and discrete element method for modelling fluid–particle interactions with experimental assessment. Int J Numer Methods Eng 2010;81:229–45.
[35] Melrose J, Ball R. The pathological behaviour of sheared hard spheres with hydrodynamic interactions. EPL 1995;32:535.
[36] FortranCL. https://code.google.com/archive/p/fortrancl.
[37] Bernaschi M, Fatica M, Melchionna S, Succi S, Kaxiras E. A flexible high-performance lattice Boltzmann gpu code for the simulations of fluid flows in complex geometries. Concurr Comput 2010;22:1–14.
[38] Clausen JR, Reasor DA, Aidun CK. Parallel performance of a Lattice–Boltzmann/finite element cellular blood flow solver on the ibm blue gene/p architecture. Comput Phys Commun 2010;181:1013–20.
[39] Mountrakis L, Lorenz E, Malaspinas O, Alowayyed S, Chopard B, Hoekstra AG. Parallel performance of an ib-lbm suspension simulation framework. J Comput Sci 2015;9:45–50.
[40] Ohern CS, Silbert LE, Liu AJ, Nagel SR. Jamming at zero temperature and zero applied stress: the epitome of disorder. Phys Rev E 2003;68:011306.
[41] Perera DN, Harrowell P. Stability and structure of a supercooled liquid mixture in two dimensions. Phys Rev E 1999;59:5721.
[42] Krieger IM, Dougherty TJ. A mechanism for non-newtonian flow in suspensions of rigid spheres. Trans Soc Rheol 1959;3:137–52.
[43] Dames B, Morrison BR, Willenbacher N. An empirical model predicting the viscosity of highly concentrated, bimodal dispersions with colloidal interactions. Rheol Acta 2001;40:434–40.
[44] Einstein A. Eine neue bestimmung der moleküldimensionen. Ann Phys 1906;324:289–306.
[45] Einstein A. Berichtigung zu meiner arbeit:eine neue bestimmung der moleküldimensionen. Ann Phys 1911;339:591–2.
[46] Brown E., Zhang H., Forman N.A., Maynor B.W., Betts D.E., Desimone J.M., Jaeger H.M. Shear thickening and jamming in densely packed suspensions of different particle shapes 84. 2011. 1–11
[47] Bergström L. Shear thinning and shear thickening of concentrated ceramic suspensions. Colloids Surf A 1998;133:151–5.
[48] Virtual prototyping of complex fluids and flowing materials. 2017. https://electricant.com/page/materials.